Operando time and space-resolved liquid-phase diagnostics reveal the plasma selective synthesis of nanographenes

Darwin Kurniawan, Francesca Caielli, Karthik Thyagajaran, Kostya Ostrikov, Wei-Hung Chiang, David Z Pai

Nanoscale Horizons

COMMUNICATION

Operando Time and Space-Resolved Liquid-Phase Diagnostics Reveal the Plasma Selective Synthesis of Nanographenes

Received 00th January 20xx,
Accepted 00th January 20xx

DOI: 10.1039/x0xx00000x

Darwin Kurniawan,[a] Francesca Caielli,[b] Karthik Thyagajaran,[b] Kostya (Ken) Ostrikov,[c] Wei-Hung Chiang,[a]* and David Z. Pai [b,d]*

Coupling atmospheric-pressure low-temperature plasmas to electrochemical reactors enables the generation of highly reactive species at plasma-liquid interfaces. This type of plasma electrochemical reactor (PEC) has been used to synthesize fluorescent nitrogen-doped graphene quantum dots (NGQDs),[1] which are usable for multifunctional applications in a facile, simple, and sustainable way. However, the synthesis mechanism remains poorly understood, as well as the location of synthesis. To research these questions, we present an *in situ* diagnostics study on liquid phase chemistry during the PEC synthesis of NGQDs from chitosan. Monitoring of the photoluminescence and UV-VIS absorption at different depths in the reaction medium during plasma treatment reveals that the NGQD production initiates at the plasma-liquid interface but its completion and/or accumulation occurs at a few millimetres depth below the interface, where the liquid ceases to flow convectively, as determined by particle image velocimetry. Our study provides insights into the plasma synthesis of fluorescent GQDs/NGQDs from carbon precursors that may prove useful for achieving the scalability of PEC processes up to continuous-flow or array reactors.

Hybridized mainly by sp^2 carbon with unique photoluminescence properties derived from quantum confinement and edge effects, graphene quantum dots (GQDs) as zero-dimensional materials have been applied to multifunctional applications including sensing,[2] imaging,[3] drug

[a] *Department of Chemical Engineering, National Taiwan University of Science and Technology, Taipei, 10607 Taiwan.*
[b] *Institut Pprime (CNRS-Université de Poitiers-ENSMA), Futuroscope Chasseneuil, F-86962, France.*
[c] *School of Chemistry and Physics and QUT Centre for Materials Science, Queensland University of Science and Technology (QUT), Brisbane, QLD, 4000 Australia.*
[d] *Laboratoire de Physique des Plasmas, CNRS, Sorbonne Université, Université Paris-Saclay, École Polytechnique, Institut Polytechnique de Paris, F-91128, Palaiseau, France.*

†Electronic Supplementary Information (ESI) available: [experimental section and OES data]. See DOI: 10.1039/x0xx00000x

New concepts

The plasma electrochemical reactor (PEC) is a combination of an atmospheric-pressure low-temperature plasma with an electrochemical reactor, which has been utilized to synthesize low-dimensional nanocarbons in a rapid, scalable, sustainable, and catalyst-free manner. Graphene quantum dots (GQDs) recently have spurred tremendous attention owing to their distinct quantum transitions and tunable bandgaps for emerging applications. However, a firm understanding of the mechanisms and location of PEC synthesis remains elusive, making it challenging to develop a scalable yet controllable method to synthesize GQDs with fine-tuned structures and properties. To address this problem, we implement various *in situ* diagnostics in this study, including optical emission, absorption, and photoluminescence spectroscopies, as well as particle image velocimetry, to examine plasma-induced liquid chemistry and transport during the synthesis of nitrogen-doped GQDs (NGQDs) from chitosan. The *operando* and space-resolved diagnostics reveal that although synthesis is initiated at the plasma-liquid interface, the production of NGQDs is completed and/or accumulated at a few millimetres depth below the interface, where the liquid flow ceases convection. This study is expected to deliver a strong and immediate impact across diverse areas of nanoscale materials synthesis, plasma physics and chemistry, and *operando* spectroscopy, with possible implications for biotic-abiotic interfaces, where *in-situ* nanoparticle formation within tissue is possible upon plasma contact with tissue interfaces.

delivery,[4] catalysis,[5] energy and photoelectronic devices.[6-8] Doping the GQDs with heteroatoms such as nitrogen (N) has been the most commonly utilized technique to enhance the performance of the aforementioned applications by improving the photoluminescence quantum yield (PLQY) and altering the electronic properties of GQDs.[1] The synthesis of nitrogen-doped graphene quantum dots (NGQDs) can be generally categorized into two basic methods: direct synthesis and post-growth doping.[6] The latter method involves the doping of N atoms into pre-synthesized GQDs and is unfavourable because of its need for strong acids, high temperature, and long reaction times, especially given the current emphasis on clean energy and global warming issues.

On the other hand, the direct synthesis of NGQDs can be further classified into top-down and bottom-up approaches.[9] The principle top-down approaches are chemical, electrochemical, or mechanical cutting of higher dimension and/or bulk N-doped graphitic carbon materials, whereas the bottom-up approach involves carbonization, pyrolysis, or step-wise chemical reactions of carbon- and nitrogen-containing chemical precursors to form NGQDs. However, the top-down approaches still require toxic and hazardous reagents, harsh reaction conditions, and long reaction times. The difficulty of structure controllability and property tenability are also the challenges often faced by these conventional top-down approaches. On the other hand, bottom-up approaches including microwave-assisted and hydrothermal techniques can offer a green and cost-effective in synthesizing NGQDs from various renewable precursors.[10-12] Moreover, with the possibility of precise control over NGQDs properties and scalability, bottom-up approaches are promising for sustainable and efficient nanomaterial syntheses.

The use of plasma electrochemical reactors (PEC) has emerged as a promising method for the bottom-up synthesis of NGQDs owing to its environmental compatibility, scalability, and simplicity.[1, 13] The PEC is composed of an atmospheric-pressure plasma in contact with an aqueous solution, producing unique physico-chemical conditions for synthesis. Low-temperature plasma chemistry leads to the formation of gas-phase species that undergo a cascade of processes in the liquid to produce aqueous reactive species such as OH radicals.[14] In addition, the plasma produces energetic photons and electrons and enhances the electric field near surfaces. Our hypothesis is that plasma-driven non-equilibrium electrochemistry enables nucleation/assembly without using reducing agents, dissociation without using acids/bases, and non-thermal reaction activation. We suspect this is the case because of our previous success in synthesizing GQDs in a single-step non-assisted process using PEC reactors.[13, 15, 16] Other studies have also reported the suitability of PECs for various colloidal nanomaterials synthesis, including GQDs and carbon dots (CDs),[17-23] as well as metal and silicon nanoparticles.[24, 25]

Despite the demonstrated ability of PECs to synthesize fluorescent carbon nanomaterials, the *in situ* liquid phase diagnostics of where and how the reaction takes place during plasma treatment has never been explored. This is a critical step towards understanding the synthesis mechanism and ultimately optimizing the process. Thus, we seek to address this need by monitoring changes in the photoluminescence (PL) and UV-VIS absorption spectra of the precursor solution at different depths in the reaction medium during plasma treatment (**Figure 1**). *In situ* PL was conducted by focusing a pulsed laser at 532 nm into the solution at different depths below the plasma-liquid interface (close to the interface (≤ 1 mm), 2, 5, and 13 mm) to excite the produced NGQDs during plasma treatment, while the exhibited PL signal was recorded using a spectrograph (Acton SP2500i) equipped with an intensified CCD camera (Princeton Instruments PIMAX4).[26] The spectrometer was constructed in-house to suppress the optical emission from the plasma discharge and provide spectral imaging capability in one dimension, as described in reference [26]. These spectroscopic measurements will be compared to the liquid flow field characterized using particle image velocimetry (PIV) performed in a cross-sectional plane through the optical cell used for *in situ* PL measurements. Both the plasma and the platinum ground wire are contained in this plane. In addition, optical emission spectroscopy (OES) was performed to characterize basic plasma properties during the reaction (**Figure 1**). The PEC-based NGQD synthesis was conducted based on our previous reports.[1, 13] Chitosan, an inexpensive and abundant biomass, was used as the sole source of both carbon and nitrogen to produce NGQDs using PECs. The detailed *in situ* diagnostics reveal that the PEC-based synthesis of NGQDs from chitosan begins at the plasma-liquid interface and the resulting NGQDs accumulate at a few millimetres depth below the interface, at the edge of the zone of convective flow. Our finding provides insights into the plasma conversion of a carbon-containing precursor into fluorescent GQDs/NGQDs, which may be applied to develop the continuous and large-scale production of GQDs/NGQDs via microfluidic technology.[27] This study may also be relevant to the study of biotic-abiotic conducting self-formed interfaces underneath tissue,[28] in which plasma contact with a tissue interface can promote direct *in situ* nanoparticles formation beneath the tissue.

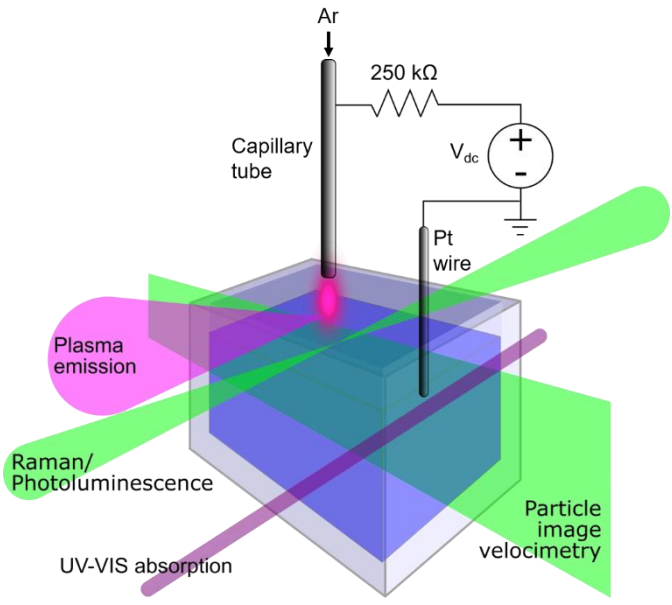

Figure 1. Schematic diagram of *in situ* diagnostics on the plasma electrochemical synthesis of NGQDs from chitosan under ambient conditions. Shown are the light paths of each diagnostic. For OES, the light emission from the plasma was directed into a UV-VIS microscope system, as shown in Darny et al.[29] A focused laser beam (λ = 532 nm) was used to obtain the photoluminescence (PL) spectrum using the microspectroscopy bench described in Pai.[26] A collimated UV-VIS light beam was used to obtain the absorption spectrum using the system described in Kurniawan et al.[13] Finally, a laser sheet (λ = 532 nm) was used for particle image velocimetry (PIV), as described in the supporting information.

The NGQDs were synthesized using PEC equipped with a direct current (DC) discharge flowing argon operated at 5 mA fixed discharge current for 1 hour under ambient conditions.[1, 13] **Figure 2** shows the materials characterization of the colloidal NGQDs. The PL spectroscopic measurement reveals the excitation-dependent emission of NGQDs that peaks at excitation and emission wavelengths of 370 and 451 nm (**Figure 2a**), respectively. The UV-Vis absorption spectrum of NGQDs presented in **Figure 2b** (black color) indicates a broad absorption peak at 282 nm and a tail from 350 – 550 nm, which correspond respectively to the π-π* transitions of C=C/C=N and n-π* transitions of the non-bonding electrons from C-O/C-N bonds.[30, 31] Hence, the maximum of emission exhibited at 370 nm excitation can be attributed to the defect n-state from the surface functional groups and N dopants, as indicated by the wavelengths of the emission maxima of both the PLE and PL spectra in **Figure 2b**. The existence of N doping and surface functional groups can be confirmed by FTIR (**Figure 2c**) and X-ray photoelectron spectroscopy (XPS) measurements (**Figure S1**). A broad band and a peak observed around 3050 – 3170 and 1384 cm^{-1} are respectively assigned to the vibrational stretching and bending of N–H groups.[4] The oxygen containing functional group is also confirmed by the occurrence of vibrational stretching of C=O and C–O at 1558 and 1076 cm^{-1}, respectively, from carboxylic (–COOH) and hydroxyl (–OH) groups,[1] which is also confirmed from the O–H stretch around 2943 – 3050 cm^{-1}. Moreover, the small peak observed around 2870 cm^{-1} is due to the vibrational stretching of C–H of the benzene ring of NGQDs, while the occurrence of C–H vibrational bending peaks around 667 – 833 cm^{-1} can be ascribed to the deformation of benzene rings caused by non-graphitic N-doping.[32] The high-resolution XPS measurement on N1s peak reveals that the N-doping exists in various configurations after fitting with Voigt profiles, including pyridinic N at 398.5 eV, amino N at 399.3 eV, pyrollic N at 399.8 eV, and graphitic N at 400.3 eV.[13] This N-doping configuration can be tailored by modulating the plasma-liquid chemistry during the synthesis.[13]

Nanoscale Horizons

COMMUNICATION

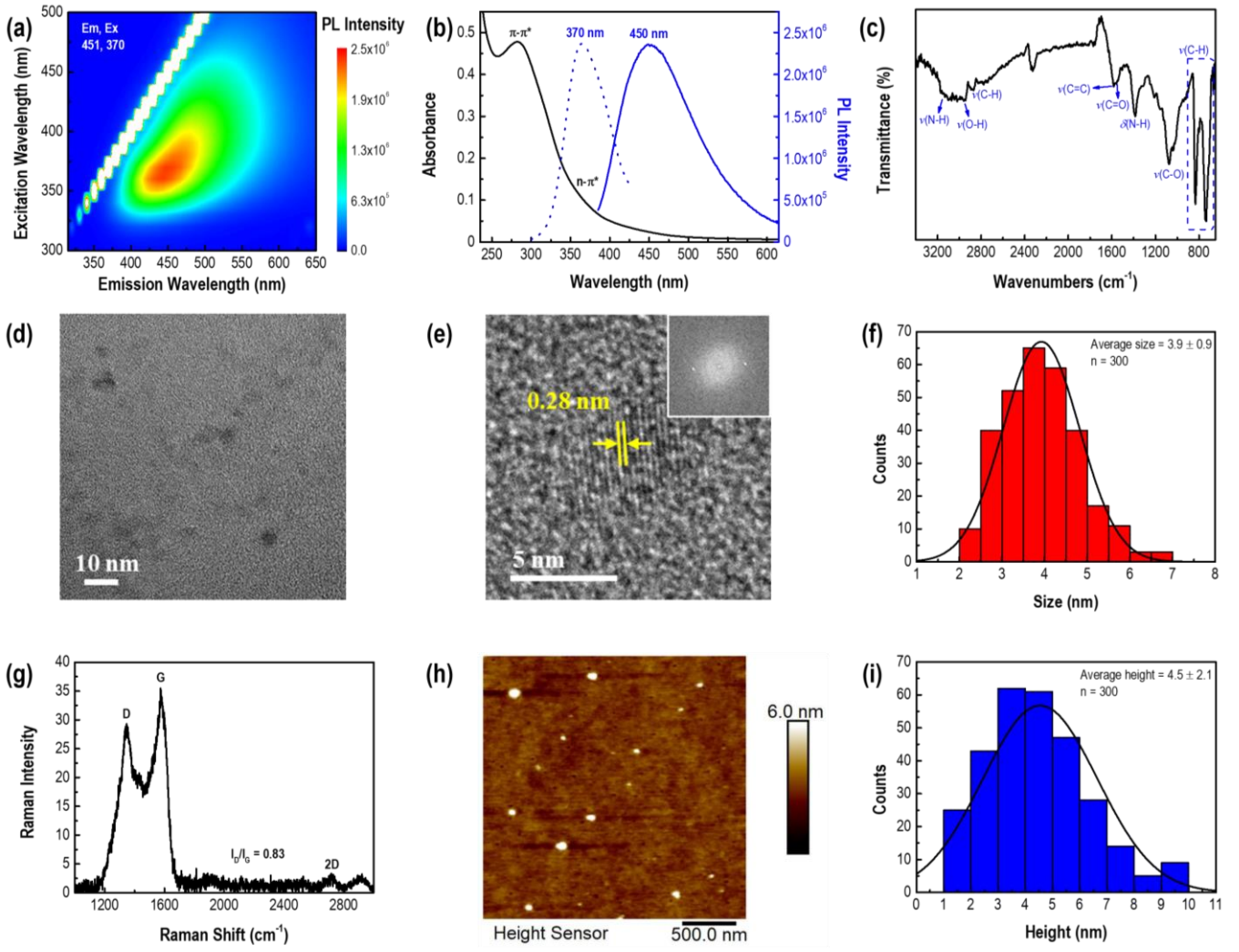

Figure 2. *Ex situ* characterizations of the synthesized NGQDs after 1 hour of plasma treatment at 5 mA. (a) PL map, (b) UV-Vis absorption (black), PLE (blue dot) and PL spectra (blue line) with emission maxima at 370 and 450 nm excitation and emission wavelengths, respectively, (c) FTIR, (d) low magnification TEM and (e) high-resolution TEM images (inset: FFT), (f) the corresponding histogram of particle size distribution from 300 different particles with a bin size of 0.5 nm, (g) microRaman, (h) AFM image, and (i) the corresponding histogram of particle height distribution from 300 different particles with a bin size of 1 nm. All the distribution histograms were fitted with a standard normal distribution.

The excitation-dependent behaviour of NGQDs shown in **Figure 2a** can be plausibly associated with the various N-dopant configurations and oxygen-containing functional groups including hydroxyl (-OH), carboxylic (-COOH), and epoxy (C-O-C) (**Figure S2c-d**).[33] These N and O functionalities can introduce new surface states with discretized energy levels. Thus, after photonic excitation, the excited electrons in the π* states can relax to the N and O surface states, followed by multiple discrete emissions during electronic relaxation from the surface states to the ground states, generating the excitation-dependent emission behaviour of NGQDs.[33]

TEM measurements were performed to understand the morphological structure of the synthesized NGQDs. The TEM image depicted in **Figure 2d** indicates the particle-like nanostructure of the synthesized NGQD. A high-resolution TEM measurement clearly reveals the lattice structure with a *d*-spacing of 0.28 nm corresponding to the (002) crystal plane of graphite (**Figure 2e**).[30] The inset in **Figure 2e** shows the FFT

image used for the calculation of the *d*-spacing. By taking a size average from at least 300 different particles and fitting with a standard normal distribution,[34] the particle size of the synthesized NGQDs was estimated to be 3.9 ± 0.9 nm. MicroRaman measurements were further performed to understand the vibrational structure of NGQDs. **Figure 2g** shows the classic D- and G-bands of graphene at 1348 and 1574 cm^{1}, respectively.[35, 36] In addition, the I_D/I_G ratio of 0.83 suggests a prominent defect structure in the synthesized NGQDs resulting from N-doping, surface functional groups, and vacancies caused by non-graphitic N-doping. Unlike single-layered highly ordered pyrolytic graphene (HOPG), the 2D-band observed at 2717 cm^{-1} is rather unpronounced which can be due to the existence of surface functional groups, N-doping, few-layer structures, and the small size of GQDs.[31, 35, 36] Indeed, the AFM measurement in **Figure 2h** confirms the average height of 4.5 ± 2.1 nm (**Figure 2i**) after averaging from 300 different particles and fitting with a standard normal distribution, suggesting that the synthesized NGQDs are composed of several layers of graphene structure.[37] The corresponding height profile of three representative dots can be seen in supporting information section S3.

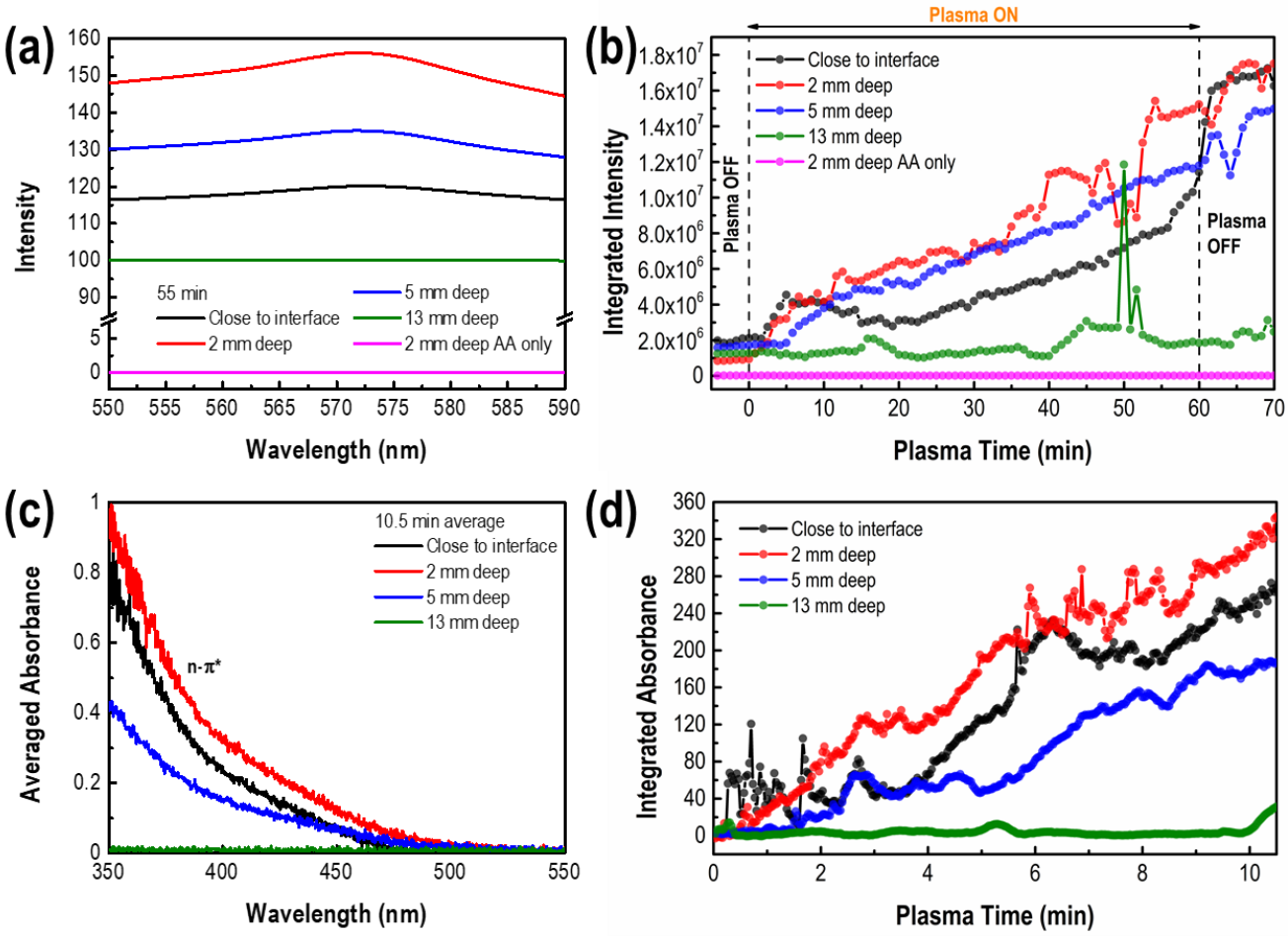

Figure 3. In situ PL and UV-Vis absorption diagnostics at different depth. (a) Representative PL spectra of colloidal NGQDs at different depths after 55 min of plasma treatment. (b) Time series of integrated PL intensity changes at different depths at 5 min before and during 60 min of plasma treatment, followed by 10 min without plasma. (c) Time-averaged absorption spectra of colloidal NGQDs at different depths after 10.5 min of plasma treatment. (d) Time series of integrated absorbance from 350 – 550 nm at different depths during 10.5 min of plasma treatment. Acetic acid is denoted as AA.

Having verified the synthesis of NGQDs, we now turn our attention to the characterization of the reaction medium using liquid-phase diagnostics. **Figure 3a** shows representative PL spectra at different depths after 55 min of plasma treatment. Interestingly, the strongest PL intensity is exhibited by the measurement at 2 mm depth, followed by 5 mm, then close to the interface (≤1 mm). Since the measurement was conducted during the course of the reaction, a time series of PL change with respect to each depth can be established, as depicted in **Figure 3b**. The PL intensities from 550 – 590 nm were integrated over the spectral range. Before plasma ignition, there was an observable PL at all depths except for the acetic acid (AA) solution without containing any chitosan. Therefore, this PL can be attributed to the PL background of chitosan solution. Just several minutes after plasma ignition, the PL intensities in the regions close to the interface and at 2 mm depth start to increase. The PL signal can be attributed to the production of fluorescent nanomaterials, namely NGQDs, or to benzene rings

contained in organic byproducts. Surprisingly, the PL intensity close to the interface does not increase monotonically, instead there is a decreasing trend from around 5 to 20 min plasma treatment before the PL intensities start to increase again. However, the PL intensities at 2 and 5 mm depths increase monotonically. For the first 15 min, negligible PL change is observed deep in the bulk liquid at 13 mm depth similar to a control study at 2 mm depth with AA solution only, which exhibited stagnant PL throughout the whole plasma process. PL fluctuation starts to occur and becomes more intense with prolonged plasma time for chitosan at 13 mm. However, the integrated intensities are relatively still almost similar to the beginning and even before plasma ignition. The control study clarifies that the NGQDs are indeed produced from chitosan and little synthesis or accumulation of products occurs at 13 mm depth.

After 60 min, the plasma was turned off, leading to two observations. First, there was a sudden increase in the PL intensities close to the interface which may partially reflect a change in fluid motion upon halting the plasma: the NGQDs residing at 2 mm depth may mix with the surface layer. Second, the PL intensity continues to increase at all depths, which implies that transport between fluid layers at different depths does not drive the increase. The increase persists for at least 10 minutes after the discharge ends, which may point to the characteristic timescale of this other process. We attribute this phenomenon to the changing solution temperature after switching off the plasma. The non-radiative decay channel induced by the emissive traps of NGQDs activates at higher temperature due to the heat generated by the plasma.[13] When the plasma turns off, the solution temperature decreases to room temperature, deactivating the emissive traps and subsequently leading to the continued increase in PL intensity.

This cooling effect is likely to be most pronounced at the plasma-liquid interface, where the liquid temperature is particularly high at t = 60 min due to localized plasma heating. Upon switching off the plasma, the temperature in this small region equilibrates rapidly with the surroundings, causing the PL intensity close to the interface to increase sharply. The PL intensity at the interface may thus reflect highly local changes in both temperature and fluid motion, as mentioned above.

Localized heating is consistent with plasma properties determined by OES. The electron number density (n_e) can be determined from the Stark broadening of the emission at 486 nm corresponding to the H_β line of the Balmer series of atomic hydrogen present in the plasma (**Figure S1**), likely produced by the dissociation of water vapor. We find a time- and space-averaged value of $n_e \approx 10^{14}$ cm^{-3}, which is similar to previously studied atmospheric-pressure DC glow discharges generated over aqueous solutions,[38, 39] for which the gas temperature in the plasma exceeds 800 K.[40] Therefore, the plasma can likely transfer significant heat by conduction or convection at the plasma-liquid interface. Other heat transfer mechanisms such as radiation, ohmic heating, and bombardment by energetic plasma species may contribute as well.

Note that the liquid temperature cannot fully explain the PL results. During the plasma treatment, the PL was more intense at 2 mm than at 5 mm. If due only to temperature, this implies that the water should be warmer at 5 mm, according to the activation of the non-radiative decay channel of NGQDs at elevated temperatures, as mentioned previously. However, because the plasma is the source of heat transfer to the solution, we expect the water at a depth of 2 mm to be warmer than at 5 mm. Instead, we propose that the NGQDs are likely produced and/or accumulated at this 2 mm depth, thus contributing to a more intense PL despite higher water temperature.

In situ absorption measurements were performed to confirm this hypothesis. **Figure 3c** shows the *in situ* time-averaged absorption spectra of the NGQDs at different depths during 10.5 min of plasma treatment. The absorption spectra, which correspond to concentration of NGQDs or molecular fragments that become the building blocks of NGQDs, suggest that the highest concentration is located at a depth of 2 mm. No NGQDs or fragments were observed in the bulk liquid (or 13 mm depth), which supports the *in situ* PL results (**Figure 3a-b**). The time series data shown in **Figure 3d** reveal that the region close to the interface possesses the highest integrated absorbance (350-550 nm) at the beginning of the reaction, which implies that the NGQDs or building blocks are indeed initially produced here or possibly precisely at the plasma-liquid interface. The near-surface absorbance remains roughly unchanged during the first 4 min of reaction before rising further. On the other hand, the absorbance at 2 mm increases steadily from the beginning. Like the PL signal, the absorbance at 2 mm depth eventually overtakes that near the surface. In fact, this occurs even sooner for the absorbance at about 2 min, rather than at about 12 min for PL. We reason this phenomenon may be due to the convective transport of NGQDs and building blocks from the region close to the interface down to 2 mm depth.

This critical depth for convective transport is corroborated by PIV (**Figure 4**). **Figure 4a** shows the electrode positions for the PIV measurement. The liquid flow pattern consists of two counter-rotating vortices that extend 2 – 3 mm in depth. Just underneath the plasma, the fluid flows upward and then diverges into surface shear flows. There is essentially no measurable flow elsewhere in the liquid volume.

Nanoscale Horizons

COMMUNICATION

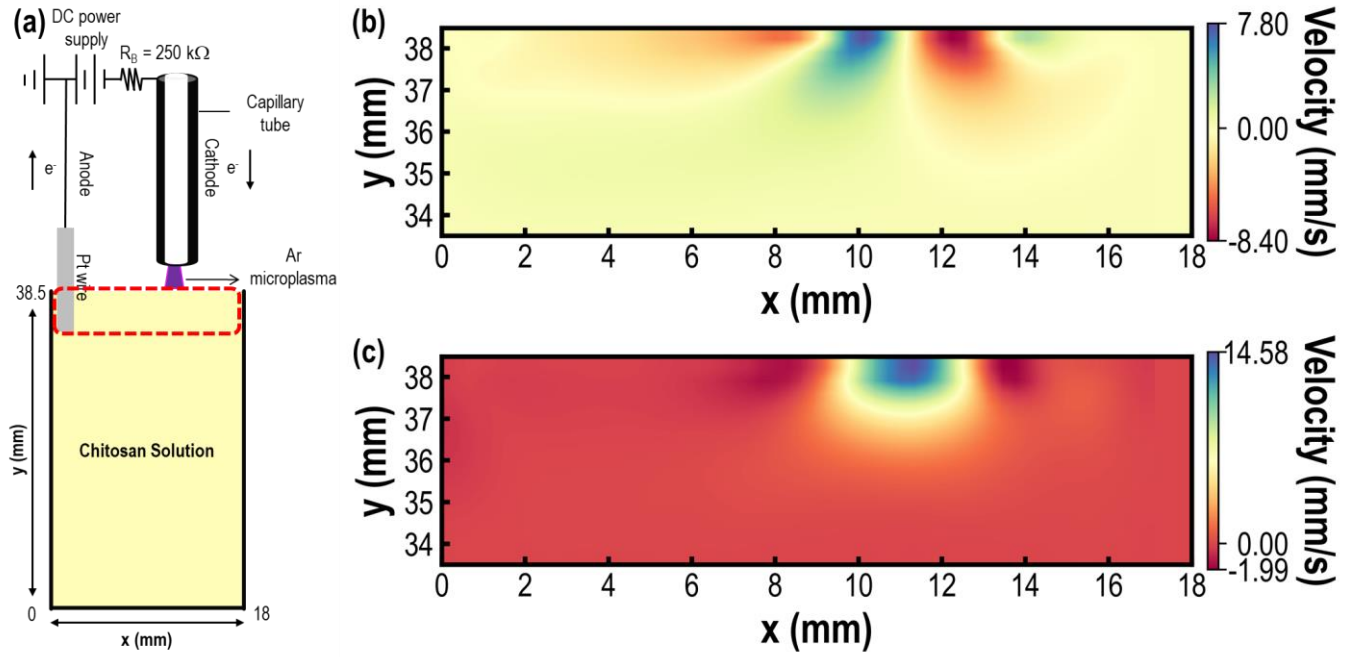

Figure 4. PIV measurement of liquid phase during NGQD synthesis from chitosan using PEC. (a) Schematic of the positions of the two electrodes during PIV measurements. The dashed red line indicates the PIV observation region shown in (b) and (c). (b) Horizontal and (c) vertical velocity components of flow field. The direction of the velocity follows the direction of incrementation of the axis. The flow fields shown represent a complete vertical cross section of the optical cell. The bottom and top of the cell is at y = 0 and y = 38.5, respectively. The discharge was located immediately above the cell at approximately x = 11. The platinum ground wire was located close to x = 0.

Based on the above observations, it is plausible that the precursor breakdown as well as NGQD nucleation and growth might be initiated at the interface or at a certain depth (≤ 1 mm) very close to the interface, yet the production of NGQDs is completed and/or accumulated at lower depth (~2 mm) below the interface due to convection by the counter-rotating vortices, schematically expressed in **Figure 5**. Near the interface, reactive species from the plasma will directly or indirectly cleave the long chain of chitosan into smaller fragments and produce NGQDs. Then, the vortices first transport the produced NGQDs away from the interface, before circulating them back around to the bottom edge of convection zone at about 2 – 3 mm depth, as illustrated in **Figure 4b-c**. Since the PL intensity at 2 mm depth is always higher than at 5 mm depth during the course of the reaction (**Figure 3b**), which is also true for the absorbance (**Figure 3d**), we may thus deduce that convective transport causes the NGQDs to accumulate in the zone within 2 mm depth. This accumulation requires a few minutes to manifest itself, with both PL intensity and absorbance becoming greater at 2 mm depth than near the surface. The accumulated NGQDs then start to diffuse deeper to at least 5 mm depth owing to the concentration difference as the main driving force. Meanwhile, the shallow transport is possibly caused by the high surface tension of the chitosan solution, however further study still needs to be conducted.

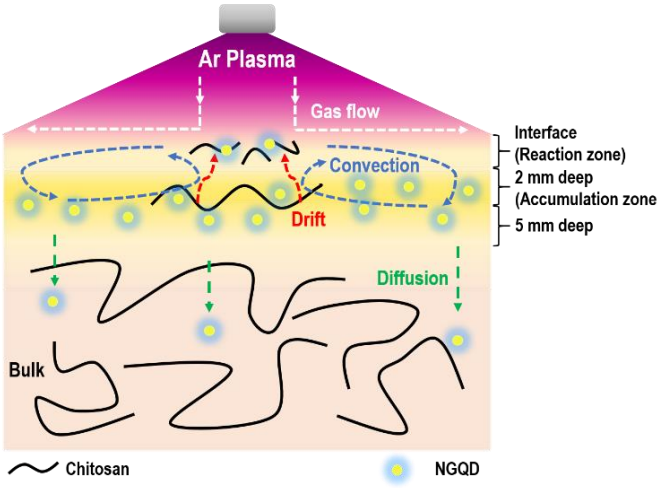

Figure 5. Illustration of mass transport during the plasma treatment of chitosan solution to form NGQDs.

It is expected that chitosan will be decomposed under plasma exposure, forming several small fragments as intermediates before reassembly into NGQDs. To identify such molecules, *ex situ* proton nuclear magnetic resonance (^{1}H NMR) measurements were performed on the plasma-treated solutions at 2-5 mm and 13 mm at different times to gain insight into the reaction mechanisms. D_2O was used as the solvent. The ^{1}H NMR results presented in **Figure S5** highlight the five regions of interest. Note that it is challenging to obtain a certain amount of solution at different depths accurately when the distance between the two depths is too small. Therefore, we only performed ^{1}H NMR measurements at two depths, 2-5 mm and 13 mm, as representative of the regions close to the interface and the bulk solution, respectively. Details about the *ex situ* ^{1}H NMR measurements can be seen in the supporting information section **S1**.

The peaks around 9.7, 8.3, and 7.0 – 7.3 ppm can be ascribed to the protons from aldehyde groups, carbonyl of formic acid, and aromatics (**Figure 6a-f**), respectively.[11, 41-43] On the other hand, the singlet peak around 4.2 ppm can be possibly attributed to the protons of methylene adjacent to the OH functional group (**Figure 6g-h**),[44] and possibly also connected to another element without having any protons such as a C atom from an aromatic compound. All the above peaks appear after 15 min of the plasma treatment and become more apparent with prolonged reaction time. Methylated fragments are also observed at a chemical shift of 1.1 – 1.3 ppm[12, 41] after 15 min of plasma treatment at 2-5 mm depth, while 30 min of plasma treatment at the 13 mm depth (**Figure S6**). However, the peaks of methylated fragments seem to be decreasing with prolonged reaction time. As a polysaccharide, chitosan is mainly constituted of several bonds, including C-C, C-O, and C-N with average bond dissociation energies of 347, 357, and 338 kJ/mol, respectively.[45] Chitosan should therefore decompose into smaller fragments when the above bond dissociation energies are reached. The thermal decomposition of chitosan generally includes depolymerisation into monosaccharides, followed by decomposition of pyranose rings via dehydration and deamination.[30]

In our case, the plasma is generated from a hollow capillary tube with an inner diameter of 180 µm. Such discharges can be expected to produce significant populations of electrons with energies exceeding 5 eV, equivalent to 480 kJ/mol.[46] This energy is in principle sufficient to promote chitosan decomposition into smaller fragments. Thus, the plasma-liquid interfacial region down to a certain depth (2-5 mm) can be expected to contain a higher number of small fragments than the bulk region, as evidenced by the faster-appearing and more pronounced aldehyde, formic acid, aromatic, and methylene peaks at 2-5 mm depth than at 13 mm (**Figure 6**). These results are in accordance with the *in situ* PL and absorption results, confirming the illustration in **Figure 5**.

Previous studies have reported that the OH radical is a highly reactive species that can cleave the glycosidic bond of long-chain chitosan into shorter chains, leading to the formation of aldehyde groups through the oxygenation of pyranose rings.[13, 47] On the other hand, plasma-generated solvated electrons can initiate carbon-carbon bond formation *via* pinacol coupling of aldehydes and ketones.[48] Therefore, based on the ^{1}H NMR results and literature reviews, we propose that the synthesis of NGQDs from chitosan may involve successive bond destruction and reconstruction reactions, which is similar to the formation of GQDs from another polysaccharide (lignin).[49] The plasma-generated OH radical will first cut the glycosidic bond of chitosan to produce aldehyde/carboxylic containing fragments (**Figure 6a-d**). Then, aided by the plasma-generated solvated electrons, those aldehyde/carboxylic containing fragments will reassemble into aromatic structures that eventually grow into nanographene (**Figure 6e-f**). Moreover, the decrease of the methylated fragments peaks in **Figure S6** with longer reaction time can also be possibly associated with the occurrence of an alkylation process into nanographene domains. Since the reactive species generated by the plasma can only penetrate to a limited depth into the solution,[50] it is possible that the observed fragments at 2-5 mm depth are due to the reaction induced by the plasma-generated reactive species, but the

fragments observed at 13 mm depth are due to the diffusion of the generated fragments from 2-5 mm depth.

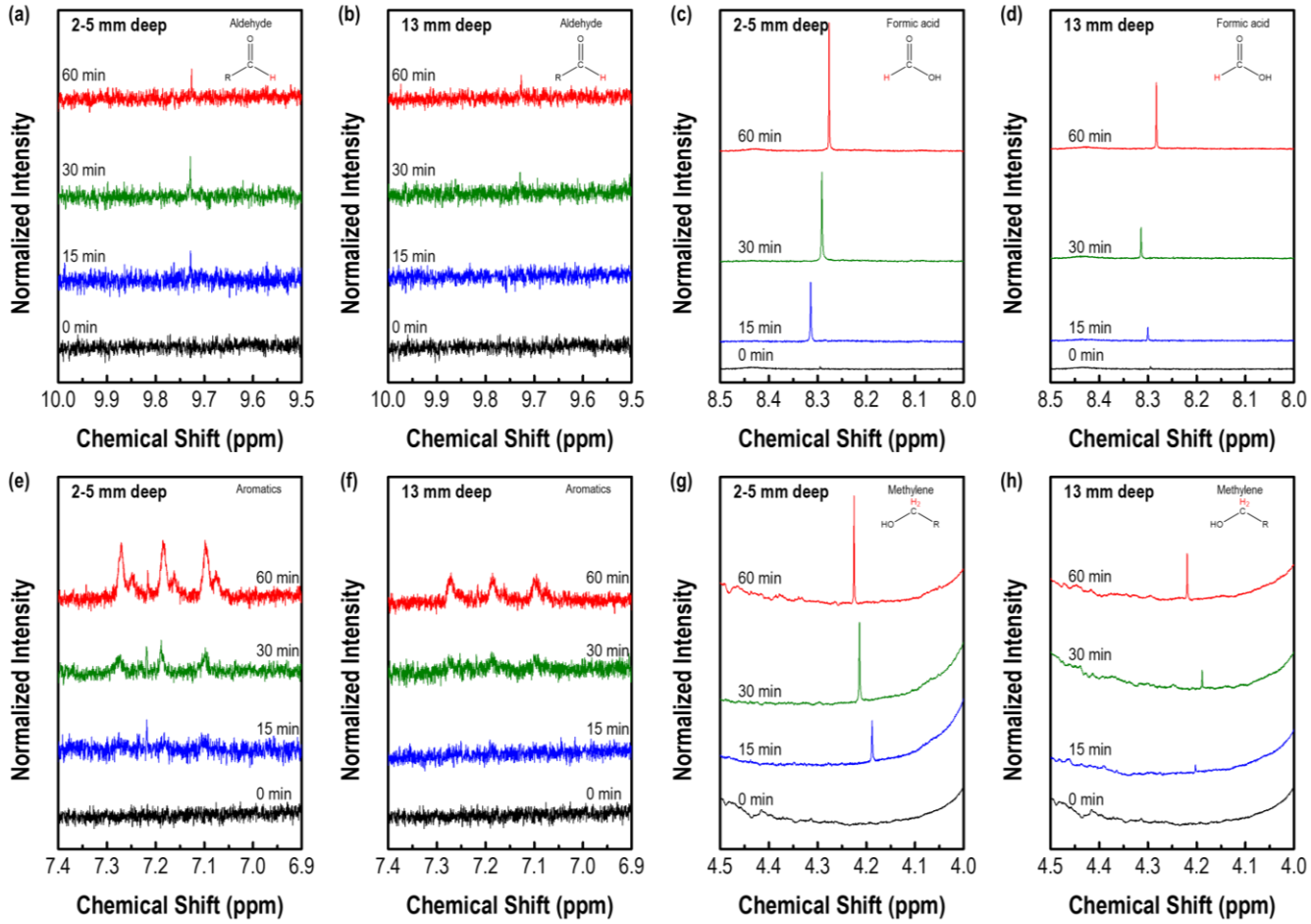

Figure 6. ***Ex situ*** **^{1}H NMR measurements of plasma-treated chitosan solution.** Magnification of ^{1}H NMR spectra in the range of (a)-(b) 9.5 – 10.0, (c)-(d) 8.0 – 8.5, (e)-(f) 6.9 – 7.4, and (g)-(h) 4.0 – 4.5 ppm of chitosan solution located at 2-5 mm and 13 mm deep into the solution after 0, 15, 30, and 60 min of the plasma treatment at 5 mA fixed discharge current.

To confirm the importance of OH radicals and solvated electrons, reactive species scavenging experiments were conducted. 2 v% of methanol and 0.1 M of H_2O_2 were used to scavenge the OH radical and solvated electrons, respectively.[16, 51] As expected, the addition of those scavengers causes a significant reduction in the absorption peak of the plasma-treated chitosan solution (**Figure S7**), confirming that both OH radicals and solvated electrons are critical for the synthesis of NGQDs.

Conclusions

In this work, we have thus identified several key structures in the aqueous solution during PEC-based synthesis of NGQDs: the interface (<1 mm depth) where the reaction mechanism is initiated, the accumulation zone (2 mm depth), and the diffusion zone (which extends to at least 5 mm depth). It is also revealed that OH radicals and solvated electrons hold an important role in cleaving the long-chain chitosan into smaller fragments, which is followed by formation into NGQDs. In a complementary study to be reported elsewhere, we will discuss the nature of the fluid flow in more detail, as well as plasma properties.

Author Contributions

D.K. performed the experiments, analysed and visualized the data, and wrote the paper. F.C. and K.T. performed the PIV measurements. K.K.O. reviewed the manuscript. W.H.C. conceived the idea, administered the project, acquired the funding, provided the resources, analysed the data, and reviewed and edited the paper. D.Z.P. conceived the idea, administered and supervised the project, acquired the funding, provided the resources, analysed and visualized the data, and wrote, reviewed and edited the paper.

Conflicts of interest

There are no conflicts to declare.

Data availability statements

The data supporting this article have been included as part of the Supplementary Information.

Acknowledgements

Financial support is gratefully acknowledged from the Agence Nationale de la Recherche programs JCJC PLASMAFACE (ANR-15-CE06-0007-01) and "Investissements d'Avenir" LABEX INTERACTIFS (ANR-11-LABX-0017-01) of the French government, the CPER-FEDER program of the Région Nouvelle Aquitaine, National Science and Technology Council (NSTC, grant nos. NSTC 111-2223-E-011-002-MY3, NSTC 111-2628-E-011-002-MY2, NSTC 109-2923-E-011-003-MY3, NSTC 111-2811-E-011-018, NSTC 111-NU-E-011-001-NU) and National Taiwan University of Science and Technology (NTUST). We also thank Romain Bellanger and Patrick Brault for technical assistance with PIV measurements at the Pprime Institute, as well as Ms. Chia-Ying Chien of NSTC (National Taiwan University) for the FE-TEM assistance. K.O. thanks the Australian Research Council (ARC) and QUT Centre for Materials Science for partial support.

References

1. D. Kurniawan and W.-H. Chiang, *Carbon*, 2020, **167**, 675-684.
2. D. Kurniawan, R.-C. Jhang, K. K. Ostrikov and W.-H. Chiang, *ACS Appl. Mater. Interfaces*, 2021, **13**, 34572-34583.
3. H. Wang, R. Revia, Q. Mu, G. Lin, C. Yen and M. Zhang, *Nanoscale Horiz.*, 2020, **5**, 573-579.
4. F. Khodadadei, S. Safarian and N. Ghanbari, *Mater. Sci. Eng. C*, 2017, **79**, 280-285.
5. T.-F. Yeh, C.-Y. Teng, S.-J. Chen and H. Teng, *Adv. Mater.*, 2014, **26**, 3297-3303.
6. Y. Du and S. Guo, *Nanoscale*, 2016, **8**, 2532-2543.
7. W. Li, H. Guo, G. Li, Z. Chi, H. Chen, L. Wang, Y. Liu, K. Chen, M. Le, Y. Han, L. Yin, R. Vajtai, P. M. Ajayan, Y. Weng and M. Wu, *Nanoscale Horiz.*, 2020, **5**, 928-933.
8. D. Kurniawan, Z. Xia, L. Dai, K. K. Ostrikov and W.-H. Chiang, *Appl. Phys. Rev.*, 2024, **11**, 021311.
9. P. Tian, L. Tang, K. S. Teng and S. P. Lau, *Mater. Today Chem.*, 2018, **10**, 221-258.
10. F. Rigodanza, M. Burian, F. Arcudi, L. Dordevic, H. Amenitsch and M. Prato, *Nat. Commun.*, 2021, **12**, 2640.
11. B. Bartolomei, A. Bogo, F. Amato, G. Ragazzon and M. Prato, *Angew. Chem. Int. Ed.*, 2022, **61**, e202200038.
12. I. J. Gómez, M. V. Sulleiro, N. Pizúrová, A. Bednařík, P. Lepcio, D. Holec, J. Preisler and L. Zajíčková, *Appl. Surf. Sci.*, 2023, **610**, 155536.
13. D. Kurniawan, R.-J. Weng, O. Setiawan, K. K. Ostrikov and W.-H. Chiang, *Carbon*, 2021, **185**, 501-513.
14. P. J. Bruggeman, M. J. Kushner, B. R. Locke, J. G. E. Gardeniers, W. G. Graham, D. B. Graves, R. C. H. M. Hofman-Caris, D. Maric, J. P. Reid, E. Ceriani, D. Fernandez Rivas, J. E. Foster, S. C. Garrick, Y. Gorbanev, S. Hamaguchi, F. Iza, H. Jablonowski, E. Klimova, J. Kolb, F. Krcma, P. Lukes, Z. Machala, I. Marinov, D. Mariotti, S. Mededovic Thagard, D. Minakata, E. C. Neyts, J. Pawlat, Z. L. Petrovic, R. Pflieger, S. Reuter, D. C. Schram, S. Schröter, M. Shiraiwa, B. Tarabová, P. A. Tsai, J. R. R. Verlet, T. von Woedtke, K. R. Wilson, K. Yasui and G. Zvereva, *Plasma Sources Sci. Technol.*, 2016, **25**, 053002.
15. J.-S. Yang, D. Z. Pai and W.-H. Chiang, *Carbon*, 2019, **153**, 315-319.
16. T. Orriere, D. Kurniawan, Y.-C. Chang, D. Z. Pai and W.-H. Chiang, *Nanotechnology*, 2020, **31**, 485001.
17. X. Huang, Y. Li, X. Zhong, A. E. Rider and K. K. Ostrikov, *Plasma Process. Polym.*, 2015, **12**, 59–65.
18. D. Carolan, C. Rocks, D. B. Padmanaban, P. Maguire, V. Svrcek and D. Mariotti, *Sustainable Energy Fuels*, 2017, **1**, 1611-1619.
19. D. H. Tung, T. T. Thuong, N. D. Cong, N. T. Liem, N. V. Kha, L. H. Manh, P. H. Minh, N. T. T. Thuy, N. M. Hoa and N. V. Phu, *Commun. Phys.*, 2018, **27**, 311-316.
20. X. Ma, S. Li, V. Hessel, L. Lin, S. Meskers and F. Gallucci, *Chem. Eng. Process.*, 2019, **140**, 29-35.
21. J. B. Joffrion, W. Clower and C. G. Wilson, *Nano-Struct. Nano-Objects.*, 2019, **19**, 100341.
22. S. D. Dsouza, M. Buerkle, B. Alessi, P. Brunet, A. Morelli, A. F. Payam, P. Maguire, D. Mariotti and V. Svrcek, *Nanotechnology*, 2023, **34**, 505601.
23. Q. H. Pho, L. L. Lin, E. V. Rebrov, M. M. Sarafraz, T. T. Tran, N. N. Tran, D. Losic and V. Hessel, *Chem. Eng. J.*, 2023, **452**, 139164.
24. G.-Y. Chang, D. Kurniawan, Y.-J. Chang and W.-H. Chiang, *ACS Omega*, 2022, **7**, 223-229.
25. D. B. Padmanaban, R. McGlynn, E. Byrne, T. Velusamy, M. Swadźba-Kwaśny, P. Maguire and D. Mariotti, *Green Chem.*, 2021, **23**, 3983-3995.
26. D. Z. Pai, *J. Phys. D: Appl. Phys.* , 2021, **54**, 355201.
27. L. Lin, H. Q. Pho, L. Zong, S. Li, N. Pourali, E. Rebrov, N. N. Tran, K. K. Ostrikov and V. Hessel, *Chem. Eng. J.*, 2021, **417**, 129355.
28. S. Inal, *Science*, 2023, **379**, 758-759.
29. T. Darny, D. Babonneau, S. Camelio and D. Z. Pai, *Plasma Sources Sci. Technol.*, 2020, **29**, 065012.
30. S. Kumar, S. K. T. Aziz, O. Girshevitz and G. D. Nessim, *J. Phys. Chem. C*, 2018, **122**, 2343-2349.
31. R. Das, S. Parveen, A. Bora and P. K. Giri, *Carbon*, 2020, **160**, 273-286.
32. C. Zhu, S. Yang, G. Wang, R. Mo, P. He, J. Sun, Z. Di, N. Yuan, J. Ding, G. Ding and X. Xie, *J. Mater. Chem. C*, 2015, **3**, 8810-8816.
33. A. B. Siddique, S. M. Hossain, A. K. Pramanick and M. Ray, *Nanoscale*, 2021, **13**, 16662-16671.
34. C. J. Murphy and J. M. Buriak, *Chem. Mater.*, 2015, **27**, 4911-4913.
35. R. Podila, J. Chacón-Torres, J. T. Spear, T. Pichler, P. Ayala and A. M. Rao, *Appl. Phys. Lett.*, 2012, **101**, 123108.
36. E. Dervishi, Z. Ji, H. Htoon, M. Sykora and S. K. Doorn, *Nanoscale*, 2019, **11**, 16571-16581.
37. C. J. Shearer, A. D. Slattery, A. J. Stapleton, J. G. Shapter and C. T. Gibson, *Nanotechnology*, 2016, **27**, 125704.
38. Y. E. Kovach, M. C. Garcia and J. E. Foster, *IEEE Trans. Plasma Sci.*, 2019, **47**, 3214-3227.
39. P. Jamróz, W. Żyrnicki and P. Pohl, *Spectrochim. Acta B: At. Spectrosc.*, 2012, **73**, 26-34.
40. Y. Lu, S. F. Xu, X. X. Zhong, K. K. Ostrikov, U. Cvelbar and D. Mariotti, *Europhys. Lett.*, 2013, **102**, 15002.
41. I. J. Gómez, M. V. Sulleiro, A. Dolečková, N. Pizúrová, J. Medalová, A. Bednařík, J. Preisler, D. Nečas and L. Zajíčková, *Mater. Chem. Front.*, 2022, **6**, 145-154.

42. S. Yang, B. Zhao, I. A. Aravind, Y. Wang, B. Zhang, S. Weng, Z. Cai, R. Li, A. Z. Baygi, A. Smith, M. A. Gundersen and S. B. Cronin, *ACS Energy Lett.*, 2021, **6**, 3924-3930.
43. Q. Zhang, R. Wang, B. Feng, X. Zhong and K. K. Ostrikov, *Nat. Commun.*, 2021, **12**, 6856.
44. Y. Kohsaka and Y. Tanimoto, *Polymers*, 2016, **8**, 374.
45. A. Buchman, H. Dodiuk, M. Rotel and J. Zahavi, in *Polymer Surfaces and Interfaces: Characterization, Modification and Application*, eds. K. L. Mittal and K.-W. Lee, VSP, Utrecht, The Netherlands, 1997, pp. 37-69.
46. S. Keniley, N. B. Uner, E. Perez, R. M. Sankaran and D. Curreli, *Plasma Sources Sci. Technol.*, 2022, **31**, 075001.
47. R. Molina, P. Jovancic, S. Vilchez, T. Tzanov and C. Solans, *Carbohydr. Polym.*, 2014, **103**, 472-479.
48. J. Wang, N. B. Üner, S. E. Dubowsky, M. P. Confer, R. Bhargava, Y. Sun, Y. Zhou, R. M. Sankaran and J. S. Moore, *J. Am. Chem. Soc.*, 2023, **145**, 10470-10474.
49. Z. Ding, F. Li, J. Wen, X. Wang and R. Sun, *Green Chem.*, 2018, **20**, 1383-1390.
50. D. Mariotti, J. Patel, V. Švrček and P. Maguire, *Plasma Process. Polym.*, 2012, **9**, 1074-1085.
51. P. Rumbach, D. M. Bartels and D. B. Go, *Plasma Sources Sci. Technol.*, 2018, **27**, 115013.